

Introduction

There are several applications that require long wavelength, large, uniform, reproducible, low cost, low $1/f$ noise, low power dissipation, and radiation hard infrared (IR) focal plane arrays (FPAs). For example, the absorption lines of many gas molecules, such as ozone, water, carbon monoxide, carbon dioxide, and nitrous oxide occur in the wavelength region from 3 to 18 μm . Thus, IR imaging systems that operate in the long wavelength IR (LWIR) region (6 - 18 μm) are required in many space applications such as monitoring global atmospheric temperature profiles, relative humidity profiles, cloud characteristics, and the distribution of minor constituents in the atmosphere which are being planned for NASA's Earth Observing System [1]. In addition, 8 - 15 μm FPAs would be very useful in detecting cold objects such as ballistic missiles in midcourse (when a hot rocket engine is not burning most of the emission peaks are in the 8-15 μm IR region) [2]. The GaAs based Quantum Well infrared Photodetector (QWIP) [3,4,5] is a potential candidate for such spaceborne and ground based applications and it can meet all of the requirements mentioned above for this spectral region.

Fig. 1 shows the schematic conduction band diagram of a typical *bound-to-continuum* QWIP [6] which utilizes bound-to-continuum intersubband absorption. By carefully designing the quantum well structure, as well as the light coupling to the detector, it is possible to optimize the material to have an optical response in the desired spectral range and determine the spectral response shape [7]. In QWIPs, the dark current originates from three different mechanisms [8]. As shown in Fig. 1, the dark current arising from the first process is due to quantum mechanical tunneling from well to well through the $\text{Al}_x\text{Ga}_{1-x}\text{As}$ barriers (sequential tunneling). This process is independent of temperature. Sequential tunneling dominates the dark current at very low temperatures ($< 30\text{ K}$). The second mechanism is thermally assisted tunneling which involves a thermal excitation and tunneling through the tip of the barrier into the continuum energy levels.

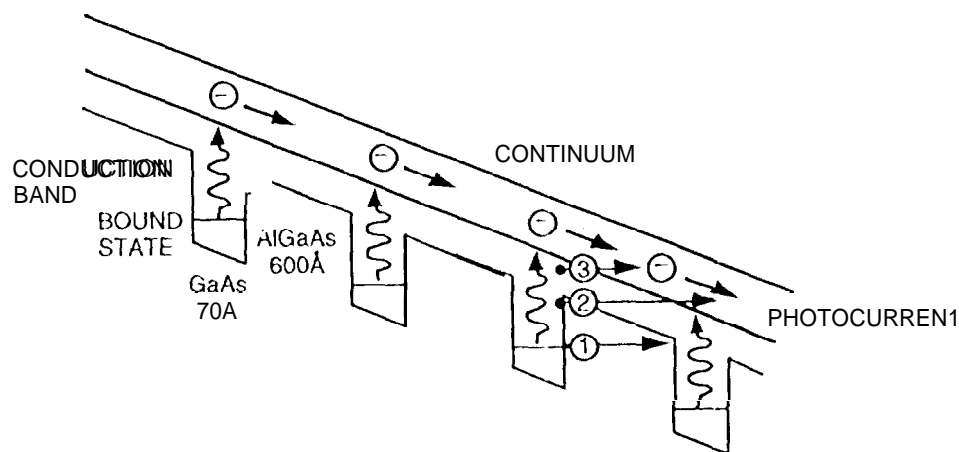


Fig. 1 Schematic diagram of the conduction band in a bound-to-continuum QWIP in an externally applied electric field. Absorption of IR photons can photo excite electrons from the ground state of the quantum well into the continuum, causing a photocurrent. Three dark current mechanisms are also shown: ground state tunneling (1); thermally assisted tunneling (2); and thermionic emission (3).

This process governs the dark current at medium temperatures. The third mechanism is classical thermionic emission and it dominates the dark current at higher temperatures (>55 K for 9 μm cutoff QWIPs). Consequently, for QWIPs operating at higher temperatures the last mechanism is the major source of dark current [8]. Therefore, the LWIR FPA we have discussed here in detail consisted of *bound-to-quasibound* QWIPs [9]. The advantage of the bound-to-quasibound QWIP over the bound-to-continuum QWIP [9] is that in the case of a bound-to-quasibound QWIP the energy barrier for thermionic emission is the same as it is for photoionization as shown in Fig. 2. In the case of the bound-to-continuum QWIP shown in Fig. 2 the energy barrier for the thermionic emission is about 6 meV less than the photoionization energy. Thus, the dark current of bound-to-quasibound QWIPs is reduced by a factor of 3 (i.e., $I_d \propto e^{-\frac{\Delta E}{kT}} \approx e^{-1}$ for $T = 70$ K) compared with bound-to-continuum QWIPs operating at the same peak wavelength.

Test Structure Results

The device structure consists of 50 periods, each period containing a 45 Å well of GaAs (doped $n = 4 \times 10^{17} \text{ cm}^{-3}$) and a 500 Å barrier of $\text{Al}_{0.3}\text{Ga}_{0.7}\text{As}$, sandwiched between 0.5 μm GaAs

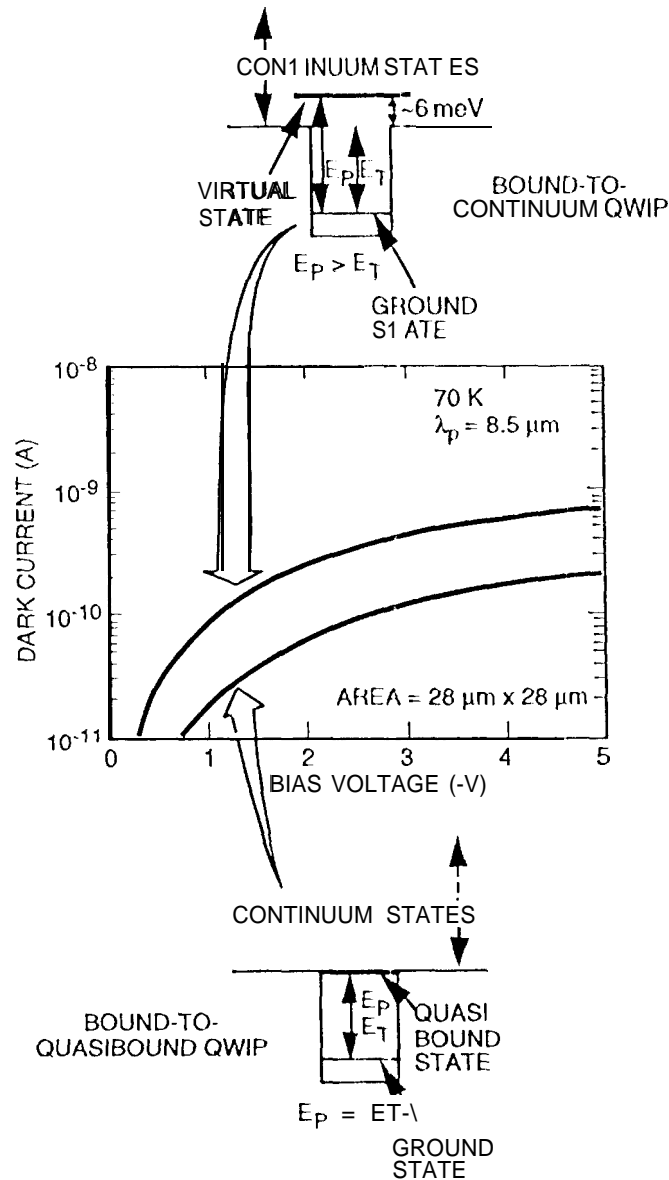


Fig. 2 Comparison of dark currents of bound-to-continuum and bound-to-quasibound LWIR QWIPs as a function of bias voltage at temperature $T = 70 \text{ K}$. Data were taken with a $200 \mu\text{m}$ diam test structure and normalized to $28 \times 28 \mu\text{m}^2$ pixel.

top and bottom contact layers doped $n = 5 \times 10^{17} \text{ cm}^{-3}$, grown on a semi-insulating GaAs substrate by molecular beam epitaxy (MBE). Then a $0.7 \mu\text{m}$ thick GaAs cap layer on top of a 300 \AA $\text{Al}_{0.3}\text{Ga}_{0.7}\text{As}$ stop-etch layer was grown *in situ* on top of the device structure to fabricate the light coupling optical cavity. The MBE grown QWIP structure was processed into $200 \mu\text{m}$ diameter mesa test structures (area = $3.14 \times 10^{-4} \text{ cm}^2$) using wet chemical etching, and Au/Ge ohmic

contacts were evaporated onto the top and bottom contact layers. The dark current-voltage curves of the QWIP were measured as a function of temperature from $T = 30$ -90 K and the $T = 70$ K curve is shown in Fig. 2 with the dark current-voltage curve of a $8.5\text{ }\mu\text{m}$ peak bound-to-continuum QWIP. The virtual excited level of this bound-to-continuum QWIP is 6 meV above the $\text{Al}_x\text{Ga}_{1-x}\text{As}$ barrier. Theoretically this should give a factor of 3 higher dark current and it closely agrees with the experimental value, of a factor of 4 higher dark current at bias $V_B = -2\text{ V}$.

The responsivity spectra of these detectors were measured using a 1000 K blackbody source and a grating monochromator. The absolute peak responsivities (R_p) of the detectors were measured using a calibrated blackbody source. The detectors were back illuminated through a 45° polished facet [7] and a responsivity spectrum is shown in Fig. 3. The responsivity of the detector peaks at $8.5\text{ }\mu\text{m}$ and the peak responsivity (R_p) of the detector is 300 mA/W at bias $V_B = -3\text{ V}$. The spectral width and the cutoff wavelength are $\Delta\lambda / \lambda = 10\%$ and $\lambda_c = 8.9\text{ }\mu\text{m}$ respectively. The bias dependent peak responsivity of the detector is shown in Fig. 4. The measured absolute peak

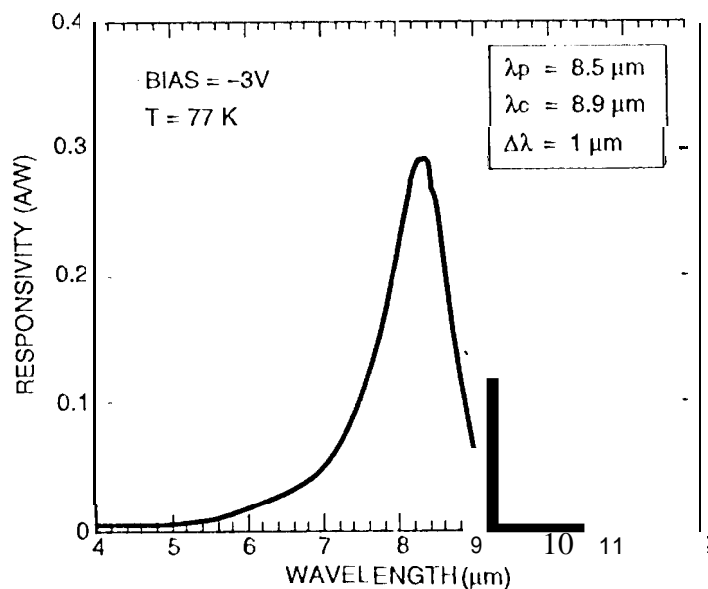


Fig. 3 Responsivity spectrum of a bound-to-quasibound LWIR QWIP test structure at temperature $T = 77\text{ K}$. The spectral response peak is at $8.5\text{ }\mu\text{m}$ and the long wavelength cutoff is at $8.9\text{ }\mu\text{m}$.

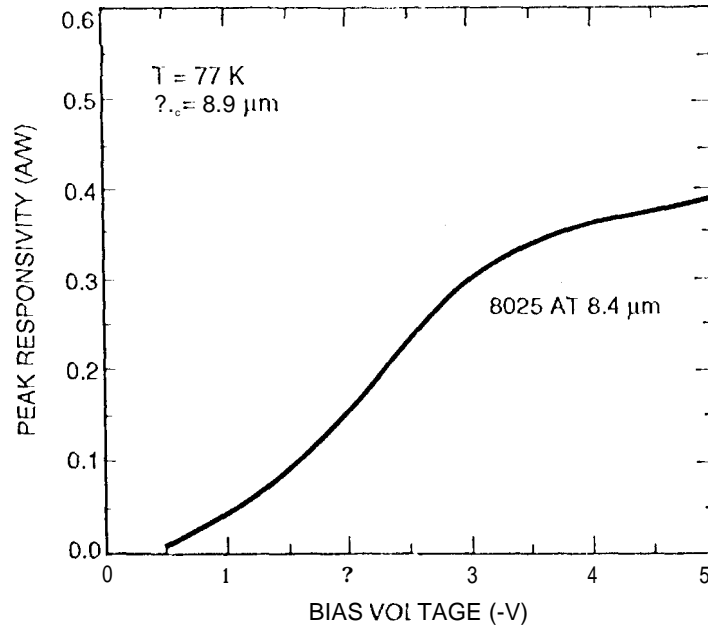


Fig. 4 Peak responsivity as a function of bias voltage at temperature $T = 77$ K.

responsivity of the detector is small up to about $V_B = -0.5$ V. Beyond that it increases nearly linearly with bias reaching $R_p = 380$ mA/W at $V_B = -5$ V. This type of behavior of responsivity versus bias is typical for a bound-to-quasibound QWIP. The peak quantum efficiency was 6.9% at bias $V_B = -1$ V (lower quantum efficiency is due to the lower well doping density) for a 45° double pass.

The current noise i_n was measured using a spectrum analyzer and the photoconductive gain g was experimentally determined using [10] $g = i_n^2 / 4 e I_D B + 1 / 2N$, where B is the measurement bandwidth and N is the number of quantum wells. The photoconductive gain of the detector reached 0.98 at $V_B = -5$ V. Since the gain of QWIP is inversely proportional to the number of quantum wells N , the better comparison would be the well capture probability p_c , which is directly related to the gain [11] by $g = 1 / N p_c$. The calculated well capture probabilities are 25% at low bias (i.e., $V_B = -1$ V) and 2% at high bias (i.e., $V_B = -5$ V) which together indicate the excellent hot-electron transport in this device structure. The peak detectivity is defined as $D_p^* = R_p \sqrt{A B} / i_n$, where R_p is the peak responsivity, A is the area of the detector and $A = 3.14 \times 10^{-4}$ cm². The

measured peak detectivity at bias $V_B = -3.2$ V and temperature $T = 70$ K is 2.3×10^{11} cm $\sqrt{\text{Hz/W}}$. These detectors show background limited performance (111.11') at bias $V_B = -2$ V and temperature $T = 72$ K for 300 K background with f/2 optics.

Light Coupling

QWIPs do not absorb radiation incident normal to the surface since the light polarization must have an electric field component normal to the layers of superlattice (growth direction) to be absorbed by the confined carriers. As shown in Fig. 6(a), when the incoming light contains no polarization component along the growth direction, the matrix element of the interaction vanishes (i.e., $\vec{\epsilon} \cdot \vec{p}_z = 0$ where $\vec{\epsilon}$ is the polarization and \vec{p}_z is the momentum along the z direction). As a consequence, these detectors have to be illuminated through a 45° polished facet [7] as shown in Fig. 6(b). Clearly, this illumination scheme limits the configuration of detectors to linear arrays

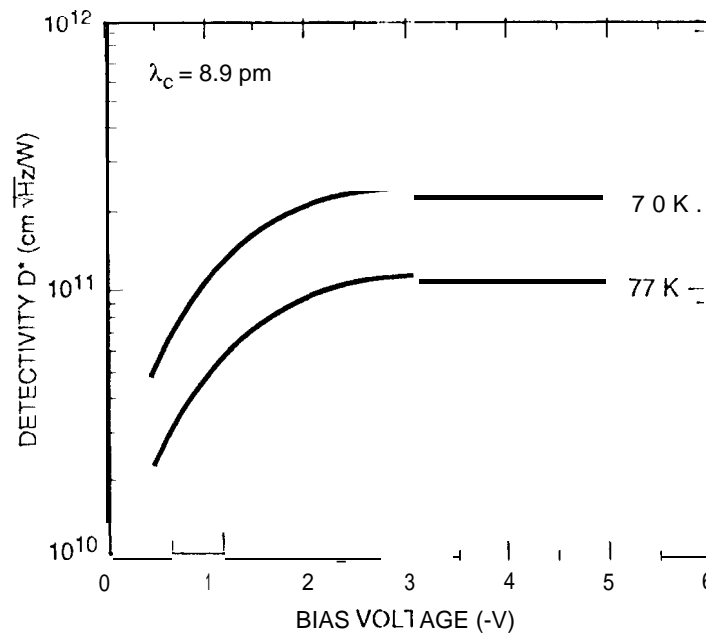


Fig. 5 Detectivity as a function of bias voltage at temperatures $T = 70$ and 77 K.

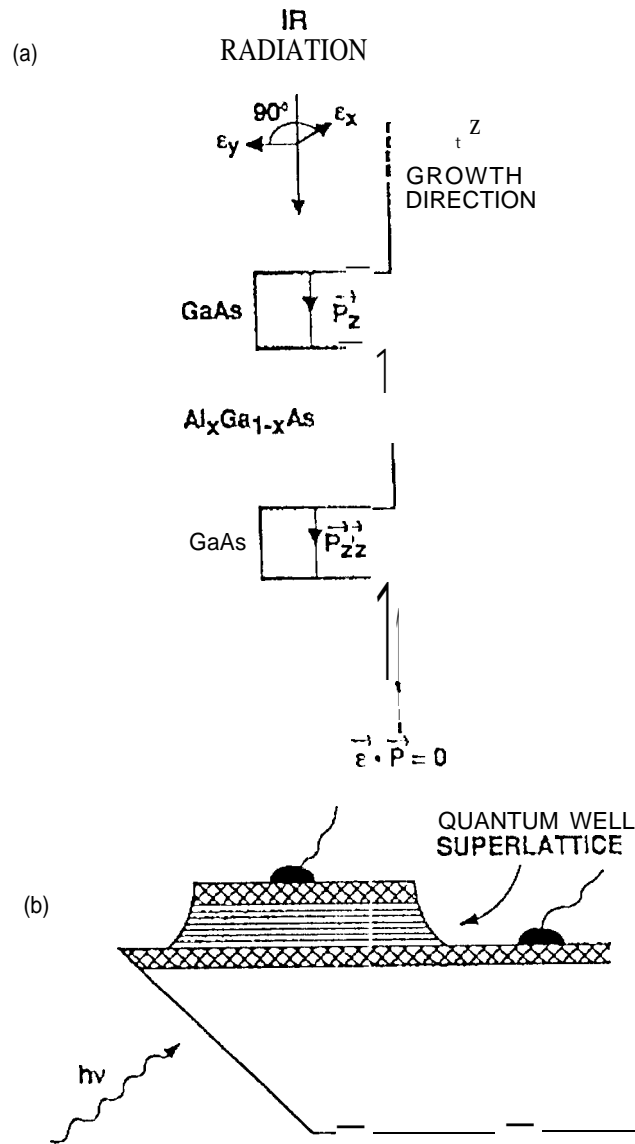


Fig. 6 (a) Intersubband absorption process of QWIPs at normal incidence. (b) 450 polished facet light coupling.

and single, elements. For imaging, it is necessary to be able to couple. light uniformly to two dimensional arrays of these detectors.

Many more passes of IR light inside the detector structure. can be obtained by incorporating a randomly roughened reflecting surface on top of the detectors which also removes the light

coupling limitations and makes two dimensional QWIP imaging arrays feasible. A factor of eight enhancement in QWIP responsivity compared to 45° illumination geometry has been achieved with a randomly roughened reflecting surface [11]. The random structure on top of the detector prevents the light from being diffracted normally backward after the second bounce as happens in the case of cross-grating. After each bounce, light is scattered at a different random angle and the only chance for light to escape out of the detector is when it is reflected towards the surface within the critical angle of the normal. For the GaAs/air interface this angle is about 17° , defining a very narrow escape cone for the trapped light. The reflector was designed with two levels of scattering surfaces located at quarter wavelength separations, as shown in Fig. 7. The area of the top unetched level is equal to the area of the etched level ($\lambda_{\text{GaAs}}/4$ deep). Therefore, the normally reflected light intensities from the top and bottom surfaces of random reflector are equal and 180° out of phase, thus maximizing the destructive interference at normal reflection and hence lowering the light leakage through the escape cone. This random structure was fabricated on the detectors by using standard photolithography and CCl_2F_2 selective dry etching. The advantage of the photolithographic process over a completely random process is the ability to accurately control the feature size and preserve the pixel to pixel uniformity which is a prerequisite for high sensitivity imaging FPAs.

imaging Arrays

Figures 7(a) and 7(b) show random reflectors on a pixel of $15\ \mu\text{m}$ cutoff 128×128 and $9\ \mu\text{m}$ cutoff 256×256 QWIP FPAs respectively. The minimum feature size of the random reflectors of $15\ \mu\text{m}$ cutoff and $9\ \mu\text{m}$ cutoff FPAs were $1.25\ \mu\text{m}$ and $0.6\ \mu\text{m}$ respectively. As shown in Fig. 7(b) the random reflectors of the $9\ \mu\text{m}$ cutoff FPA were less sharp and had fewer scattering centers compared to Fig. 7(a) due to the difficulties associated with sub-micron photolithography. After the random reflector array was defined by the lithography and dry etching, the photoconductive QWIPs of the 256×256 FPAs were fabricated by wet chemical etching through the photosensitive

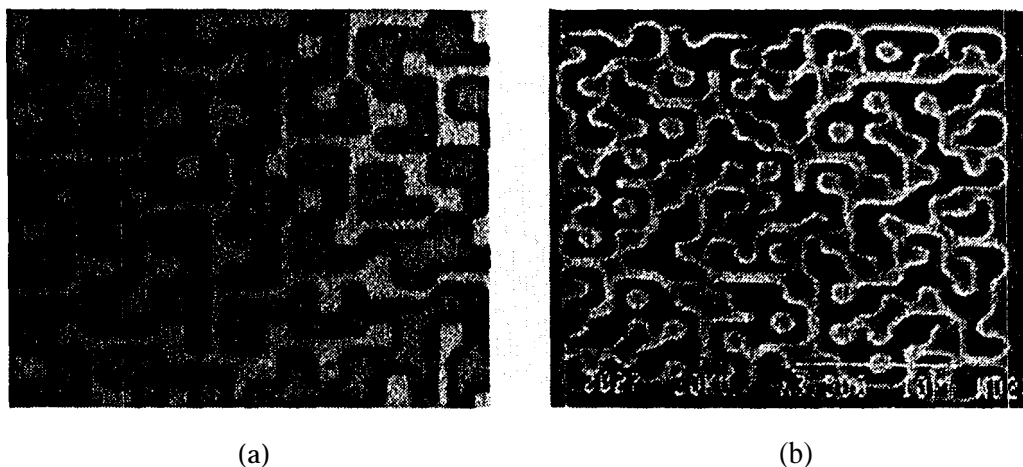


Fig. 7 (a) Two level random reflector on a pixel ($38 \times 38 \mu\text{m}^2$) of $15 \mu\text{m}$ cutoff QWIP FPA. The minimum feature size is $1.25 \mu\text{m}$. (b) Two level random rejector on a pixel ($28 \times 28 \mu\text{m}^2$) of $9 \mu\text{m}$ cutoff QWIP FPA. The minimum feature size is $0.6 \mu\text{m}$. This random reflector is less sharp and has fewer scattering centers when compared to Fig. 7(a) due to the difficulties associated with sub-micron photolithography.

GaAs/ $\text{Al}_x\text{Ga}_{1-x}\text{As}$ multi-quantum well layers into the $0.5 \mu\text{m}$ thick eloped GaAs bottom contact layer. The pitch of the FPA is $38 \mu\text{m}$ and the actual pixel size is $28 \times 28 \mu\text{m}^2$. The random reflectors on top of the detectors were then covered with Au/Ge and Au for Ohmic contact and reflection. Figure 8 shows twenty five processed QWIPFPAs on a 3 inch GaAs wafer. Indium bumps were then evaporated on top of the detectors for Si readout circuit (ROC) hybridization. A single QWIP

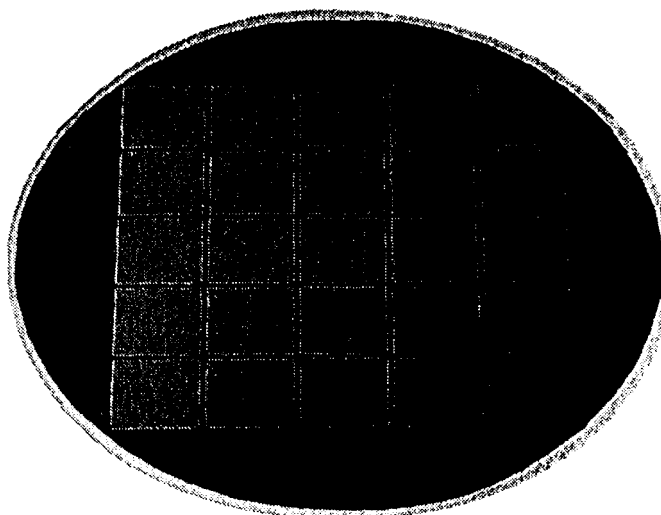


Fig. 8 Twenty-five 256×256 QWIP focal plane arrays on a 3 in. GaAs wafer

FPA was chosen and hybridized (via indium bump-bonding process) to a 256x256 CMOS multiplexer (Amber AE-166) and biased at $V_B = -1.0$ V. At temperatures below 72 K, the signal to noise ratio of the system is limited by array non-uniformity, multiplexer readout noise, and photo current (photon flux) noise. At temperatures above 72 K, temporal noise due to the QWIP's higher dark current becomes the limitation. As mentioned earlier this higher dark current is due to thermionic emission and thus causes the charge storage capacitors of the readout circuitry to saturate. Since the QWIP is a high impedance device, it should yield a very high charge injection coupling efficiency into the integration capacitor of the multiplexer. In fact Bethea et al. [3] have demonstrated charge injection efficiencies approaching 90%. Charge injection efficiency can be obtained from [4]

$$\eta_{inj} = \frac{g_m R_{Det}}{1 + g_m R_{Det}} \left[1 - \frac{1}{1 + \frac{\omega C_{Det} R_{Det}}{1 + g_m R_{Det}}} \right] \quad (1)$$

where g_m is the transconductance of the MOSFET and it is given by $g_m = eI_{Det}/kT$. The differential resistance R_{Det} of the pixels at -1 V bias is 4.5×10^{10} Ohms at $T = 70$ K and detector capacitance C_{Det} is 3.0×10^{-14} F. The detector dark current $I_{Det} = 14$ pA under the same operating conditions. According to equation (1) the charge injection efficiency $\eta_{inj} = 99\%$ at a frame rate of 30117. The FPA was back-illuminated through the flat thinned substrate membrane (thickness ≈ 1300 Å). This initial array gave excellent images with 99.98% of the pixels working (number of dead pixels ≈ 10), demonstrating the high yield of GaAs technology.

We have used the following equation to calculate the noise equivalent temperature difference NEAT of the FPA.

$$NE\Delta T = \frac{\sqrt{AB}}{D_B^* (dP_B/dT) \sin^2(\theta/2)} \quad (2)$$

where D_B^* is the blackbody detectivity, dP_B / dT is the derivative of the integrated blackbody power with respect to temperature, and θ is the field of view angle [i.e., $\sin^2(\theta/2) = (4f^2+1)^{-1}$, where f is the f number of the optical system]. Figure 9 shows the NEAT of the FPA estimated from test structure data as a function of temperature for bias voltages $V_B = -1, -2$, and -3 V. The background temperature $T_B = 300$ K, the area of the pixel $A = (28 \mu m)^2$, the f number of the optical system is 2, and the frame rate is 30117. The measured mean NEAT of the FPA was 25 mK at an operating temperature of $T = 70$ K and bias $V_B = -1$ V for 300 K background. This reasonably agrees with our estimated value of 25 mK based on test structure data. The peak quantum efficiency of the FPA was 3% (much lower quantum efficiency than expected can be attributed to the poor grating fill factor) and this corresponds to an average of 3 passes of IR

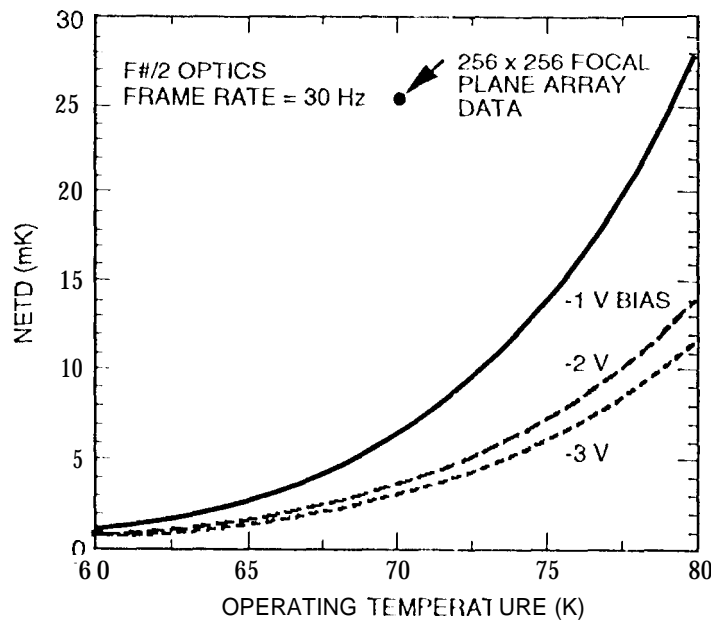


Fig. 9 Noise equivalent temperature difference NEAT estimated from test structure data as a function of temperature for bias voltages $V_B = -1, -2$, and -3 V. The background temperature $T_B = 300$ K and the area of the pixel $A = (28 \mu m)^2$. The measured NEAT of the focal plane array is 25 mK at an operating temperature of 70 K and bias $V_B = -1$ V.

radiation (equivalent to a single 45° pass) through the photosensitive multi-quantum well region. As shown in Fig. 10 the uncorrected photocurrent non-uniformity (which includes a 1 % non-uniformity of ROC and a 1.4% non-uniformity due to the cold-stop not yielding the same field of view to all the pixels in the FPA) of the 65,536 pixels of the 256×256 FPA is about 6.8% ($= \text{sigma}/\text{mean}$). The non-uniformity after two-point (17° and 27° Celsius) correction was 0.05%. As mentioned earlier this high yield is due to the excellent GaAs growth uniformity and the mature GaAs processing technology.

Hand-held QWIP Camera

A 256×256 QWIP FPA hybrid was mounted on to a 450 mW integral Sterling closed-cycle cooler assembly and installed into an Amber RADIANCE 1 TM camera-body, to demonstrate a hand-held LWIR camera (shown in Fig. 11). The camera is equipped with a 32-bit floating-point

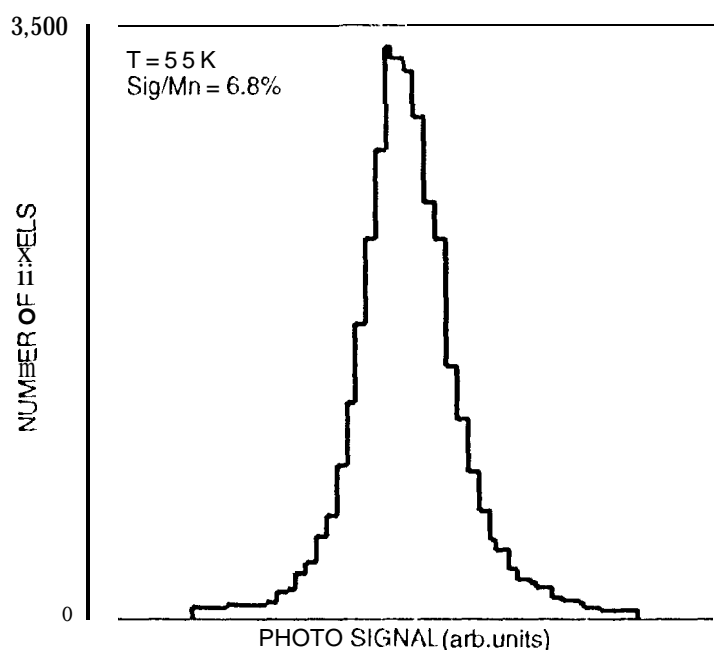


Fig. 10 Photosignal histogram of the 65,536 pixels of the 256×256 array showing a high uniformity of the FPA. The uncorrected non-uniformity ($= \text{standard deviation}/\text{mean}$) of the FPA is only 6.8% including 1% non-uniformity of ROC and 1.4% non-uniformity due to the cold-stop not being able to give the same field of view to all the pixels in the FPA.

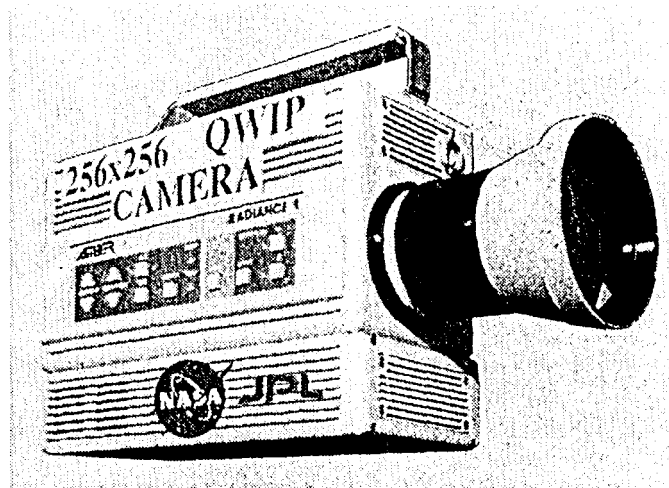


Fig. 11 Picture of the first 256x256 hand-held long wavelength QWIP camera (QWIP RADIANCE).

digital signal processor combined with multi-tasking software, providing the speed and power to execute complex image-processing and analysis functions inside the camera body itself. The other element of the camera is a 100 mm focal length germanium lens, with a 5.5 degree field of view. It is designed to be transparent in the 8-12 μm wavelength range, to be compatible with the QWIP's 8.5 μm operation. The digital acquisition resolution of the camera is 12-bits. Its nominal power consumption is less than 50 Watts.

The measured mean NEAT of the QWIP camera is 40 mK (the higher NEAT is due to the lens assembly cutting the light transmission by 35%) at an operating temperature of $T = 70\text{ K}$ and bias $V_B = -1.5\text{ V}$, for a 300 K background. The peak quantum efficiency of the FPA is 3%, corresponding to an average of 3 passes of IR radiation through the photosensitive multi-quantum well region. The low quantum efficiency can be partly attributed to the fact that the substrate reflects 30% of the light striking it; and the fact that the array has a 65% fill factor, i.e., the detectors cover only 65% of the array surface, with the remaining 35% being the dead space between detectors. The uncorrected photocurrent non-uniformity (which includes a 1 % non-uniformity of the ROC and a 1.4% non-uniformity due to the cold-stop in front of the FPA not

yielding the same field of view to all the pixels) of the 65,536 pixels of the 256x256 FPA is about 6.8% (σ/μ). The non-uniformity after two-point (17° and 27° Celsius) correction improves to an impressive 0.05%. As mentioned earlier, this high yield is due to the excellent GaAs growth uniformity and the mature GaAs processing technology.

Video images were taken at a frame rate of 60 Hz at temperatures as high as $T = 70$ K, using a ROC capacitor having a charge capacity of 9×10^6 electrons (the maximum number of photoelectrons and dark electrons that can be counted in the time taken to read each detector pixel). Figure 10 (a) shows one frame of a video image taken with a 9 μm cutoff 256x256 QWIP camera at night. The van shown in the picture was about one mile away from the camera. Figure 12 (b) shows an absorption image of acetone fumes (acetone has a strong IR absorption at 8.8 μm) taken with the same camera. These images demonstrate the high sensitivity of the 256x256 QWIP staring array camera.

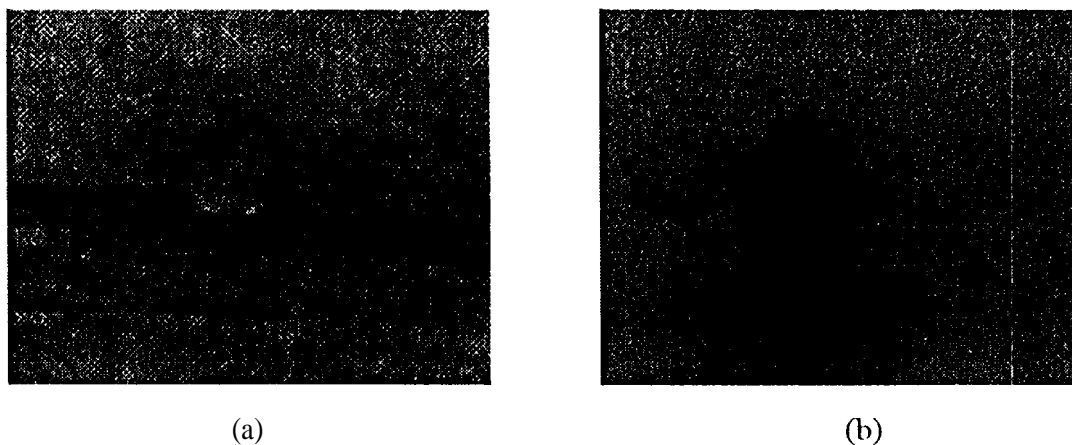


Fig. 12 (a) Shows one frame of a video image taken with a 9 μm cutoff 256x256 QWIP camera at night. The van shown in the picture was about one mile away from the camera. (b) An absorption image of acetone fumes (acetone has a strong IR absorption at 8.8 μm) taken with the same camera.

Summary

Exceptionally rapid progress has been made in the development of long wavelength QWIPs, since they were first experimentally demonstrated several years ago. It is now possible for QWIPs to achieve excellent performance (e.g., detectivities as high as $D^* = 1 \times 10^{11} \text{ cm}^2/\text{Hz/W}$ at 70 K for a 9 μm QWIP) and be fabricated into large inexpensive low-noise imaging arrays. A 70 K operating temperature can be easily achieved by single-stage Stirling cycle coolers, which allows us to demonstrate the first hand-held 256x256 FPA I.WIR camera based on QWIPs. Weighing about ten pounds, the QWIP RADIANCE camera is entirely self-contained, with no extra boxes for control, cooling, or image processing. Its sharp, inexpensive, large, uniform, infrared eye (which can be tailored to see a particular IR wavelength) makes the QWIP hand-held camera the best and the most cost-effective new tool for imaging and spectroscopy in the interesting 8-14 μm wavelength range.

Acknowledgments

The research described in this paper was performed by the Center for Space Microelectronics Technology, Jet Propulsion Laboratory, California Institute of Technology, and was jointly sponsored by the BMDO/IS&T Office, and the NASA Office of Space Access and Technology.

References

- [1] M. T. Chahine, "Sensor requirements for Earth and Planetary Observations," *Proceedings of Innovative Long Wavelength Infrared Detector Workshop*, Pasadena, California, pp. 3-31, April 24-26, 1990.
- [2] D. Du ston, "BMDO's IS&T faces new hi-tech priorities," *BMD Monitor*, pp. 180-183, May 19, 1995.
- [3] C. G. Bethea, B. F. Levine, M. T. Asom, R. E. Leibenguth, J. W. Stayt, K. G. Glogovsky, R. A. Morgan, J. D. Blackwell, and W. J. Parrish, "Long Wavelength Infrared 128 x 128 Al_xGa_{1-x}As/GaAs Quantum Well Infrared Camera and imaging System," *IEEE Trans. Electron. Devices*, vol. 40, pp. 1957-1963, 1993.
- [4] L. J. Kozlowski, G. M. Williams, G. J. Sullivan, C. W. Farley, R. J. Andersson, J. Chen, D. T. Cheung, W. E. Tennant, and R. E. DeWames, "LWIR 128x128 GaAs/AlGaAs Multiple Quantum Well Hybrid Focal Plane Array," *IEEE Trans. Electron. Devices*, vol. ED-38, pp. 1124-1130, 1991.
- [5] W. A. Beck, T. S. Faska, J. W. Little, J. Albritton, and M. Sensiper, *Proceedings of the Second international Symposium on 2-20 μm Wavelength Infrared Detectors and Arrays: Physics and Applications*, October 10-12, 1994, Miami Beach, Florida.
- [6] B. F. Levine, C. G. Bethea, G. Hasnain, V. O. Shen, E. Pelve, R. R. Abbott, and S. J. Hsieh, "High sensitivity low dark current 10 μm GaAs quantum well infrared photodetectors," *Appl. Phys. Lett.*, vol. 56, pp. 851-853, 1990.

- [7] S. D. Gunapala and K. M. S. V. Bandara, *Physics of Thin Films*, Academic Press, 21, 113 (1995), and references therein.
- [8] Sarath Gunapala, Gabby Sarusi, Jin Park, True-1 Lin, and Barry Levine, "Infrared Detectors Reach New Lengths," *Physics World*, pp. 35-40, December, 1994.
- [9] S. D. Gunapala, J. S. Park, G. Sarusi, T. L. Lin, J. K. Liu, P. D. Maker, R. E. Muller, C. A. Shott, T. Hoelzer, and B. F. Levine "128 x 128 GaAs/Al_xGa_{1-x}As Quantum Well Infrared Photodetector Focal Plane Array for imaging at 15 μ m," submitted to *IEEE Electron Device Letters*.
- [10] W. A. Beck, "Photoconductive gain and generation-recombination noise in multiple-quantum-well infrared detectors," *Appl. Phys. Lett.*, vol. 63, pp. 3589-3591, 1993.
- [11] G. Sarusi, B. F. Levine, S. J. Pearton, K. M. S. V. Bandara, and R. E. Leibenguth, "improved performance of quantum well infrared photodetectors using random scattering optical coupling," *Appl. Phys. Lett.*, vol. 64, pp. 960-962, 1994.